


Cite this: *RSC Adv.*, 2023, 13, 14849

# Synaptic plasticity realized by selective oxidation of $\text{TiS}_3$ nanosheet for neuromorphic devices†

Jing-Kai Qin,<sup>a</sup> Hai-Lin Sun,<sup>a</sup> Pei-Yu Huang,<sup>a</sup> Yang Li,<sup>b</sup> Liang Zhen<sup>ab</sup> and Cheng-Yan Xu<sup>\*ab</sup>

Memristive devices operating analogous to biology synapses demonstrate great potential for neuromorphic applications. Here, we reported the space-confined vapor synthesis of ultrathin titanium trisulfide ( $\text{TiS}_3$ ) nanosheets, and subsequent laser manufacturing of a  $\text{TiS}_3$ – $\text{TiO}_x$ – $\text{TiS}_3$  in-plane heterojunction for memristor applications. Due to the flux-controlled migration and aggregation of oxygen vacancies, the two-terminal memristor demonstrates reliable “analog” switching behaviors, in which the channel conductance can be incrementally adjusted by tuning the duration and sequence of programming voltage. The device allows the emulation of basic synaptic functions, featuring excellent linearity and symmetry in conductance change during long-term potentiation/depression processes. The small asymmetric ratio of 0.15 enables it to be integrated into a neural network for the pattern recognition task with a high accuracy of 90%. The results demonstrate the great potential of  $\text{TiS}_3$ -based synaptic devices for neuromorphic applications.

Received 6th February 2023

Accepted 9th May 2023

DOI: 10.1039/d3ra00782k

rsc.li/rsc-advances

## Introduction

Neuromorphic computing inspired by the human brain is expected to overcome the bottleneck of storage and power consumption in conventional von Neumann computing systems.<sup>1–5</sup> As the most important cornerstone of neuromorphic computing hardware architecture, the memristor operates analogous to biology synapses, in which the conductance can be incrementally modified by controlling the charge or flux through it.<sup>6–9</sup> A wealth of materials have been developed for the device implementation of memristors. Among them, two-dimensional (2D) layered semiconductors stand out because of their outstanding electrical and optoelectrical properties. Titanium trisulfide ( $\text{TiS}_3$ ) has been reported as a 2D semiconductor with strong in-plane anisotropy. It reveals a direct electric band gap of 1.0 eV, and an extremely high electron mobility more than  $10\,000\text{ cm}^2\text{ V}^{-1}\text{ s}^{-1}$  has been predicted by *ab initio* calculations.<sup>10–12</sup> However, the difference in the Ti–S bond length results in highly-aligned 1D chains with strong in-plane anisotropy,<sup>13</sup> thus the traditional synthesis methods typically yield quasi-1D nanowires or nanoribbons, which causes a great challenge for integration with other 2D materials.

Note that titanium oxide ( $\text{TiO}_x$ ) has been well studied as candidate of memristor to construct artificial synapses.<sup>14–16</sup> The migration and diffusion process of oxygen ions enable the modulation of electrical conductance, thus allowing the mimicking of synaptic functions of biology neurons, such as short-term plasticity (STP), long-term plasticity (LTP), pulse-paired facilitation (PPF),<sup>17,18</sup> *etc.* Previous studies have revealed the feasibility of controllably oxidation technique to create 2D oxide and related heterostructures,<sup>19,20</sup> thus it is expected that  $\text{TiO}_x$  and related heterostructures can also be achieved in 2D configuration based on 2D  $\text{TiS}_3$  nanosheets. The 2D  $\text{TiS}_3$ – $\text{TiO}_x$  heterostructure can be easily integrated with silicon platform and other 2D materials, and be applied for constructing synaptic device multiple functions.

In this work, we reported the space-confined synthesis of ultrathin  $\text{TiS}_3$  nanosheets with high crystalline quality. Top-gated field effect transistor (FETs) based on  $\text{TiS}_3$  nanosheet delivers a large on-state current density of  $510\text{ mA mm}^{-1}$  and high carrier mobility close to  $100\text{ cm}^2\text{ V}^{-1}\text{ s}^{-1}$ . By using a laser-assisted manufacture technique, in-plane  $\text{TiS}_3$ – $\text{TiO}_x$ – $\text{TiS}_3$  heterojunction can be created for memristor construction, which demonstrates excellent synaptic characteristics with tunable and multiple resistance levels. The device can also be integrated into neural network for high-accuracy pattern recognition. The results indicate that  $\text{TiS}_3$ -based memristors might be ideal building blocks for a neuromorphic computing system.

## Results and discussion

Atomically thin  $\text{TiS}_3$  nanosheets were obtained through a space-confined chemical vapor transport (SC-CVT) method,<sup>13</sup> where

<sup>a</sup>Sauvage Laboratory for Smart Materials, School of Materials Science and Engineering, Harbin Institute of Technology (Shenzhen), Shenzhen 518055, China. E-mail: cy\_xu@hit.edu.cn

<sup>b</sup>MOE Key Laboratory of Micro-System and Micro-Structures Manufacturing, Harbin Institute of Technology, Harbin 150080, China

† Electronic supplementary information (ESI) available. See DOI: <https://doi.org/10.1039/d3ra00782k>



the confined space can be created by stacking two freshly-exfoliated mica substate vertically (Fig. 1a). Stoichiometric Ti powders and S powders were sealed at the end of a quartz tube with pressure less than 10 mbar, and amount of  $I_2$  was also added as transport agent. The quartz tube was then heated at 550 °C for 1 h. After cooling,  $TiS_3$  nanosheets with thicknesses ranging from 8 to 30 nm can grow on the surface of sandwiched mica sheets. The as-synthesized samples on mica substrate present a small thickness in the range from 6 to 30 nm. Fig. 1b show an optical microscopy (OM) and corresponding atomic force microscopy (AFM) images of a 14 nm-thick  $TiS_3$  nanosheet, which demonstrate an atomically-flat surface. The Raman spectrum was also collected from the sample (Fig. 1c). Four active Raman modes were clearly detected, located at 176, 298, 370, and 556  $cm^{-1}$ , respectively. This is in well consistence with previously reported  $TiS_3$  crystal and nanowires,<sup>21–23</sup> further confirming the phase of  $TiS_3$  nanosheets.

We first investigated the electrical transport properties of  $TiS_3$  nanosheet by constructing a top-gated field effect transistor (FETs). To provide effective gate controlling of channel conductance, a 10 nm-thick h-BN flake serving as gate dielectric was exfoliated on the top of  $TiS_3$  nanosheet with thickness of 8 nm for device fabrication (Fig. 2a). Au/Ti (50/10 nm) electrodes are patterned and deposited through the standard laser direct writing lithography and metal deposition processes, and the channel length is set to be 5  $\mu m$ . All the electrical measurements are conducted in a Lakeshore probe station connected to a Keithley 4200A parameter analyser under dark and high vacuum conditions. Fig. 2b shows the OM image of a just-fabricated device. The linear  $I_{ds}-V_{ds}$  characteristics indicates that near ohmic contacts are formed at heterojunction between  $TiS_3$  nanosheet and Ti/Au electrodes (Fig. 2c). The transfer curves of the same device are shown in Fig. 2d. We can see that the device presents typical n-type transport behavior with a high current on-off ratio about  $10^5$ , together with a large on-state current density up to

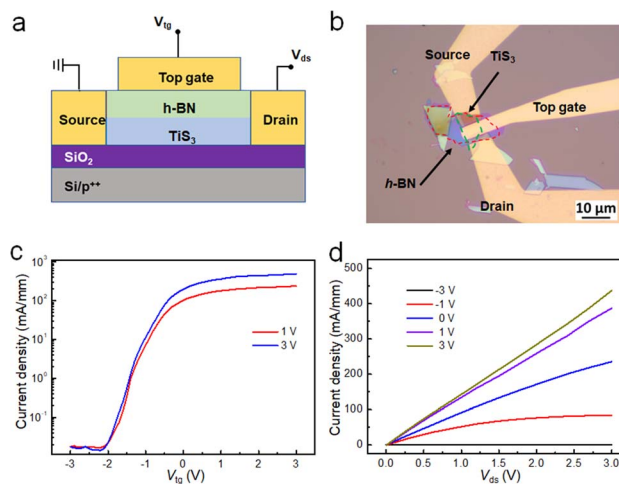


Fig. 2 Electrical performance of top-gated  $TiS_3$  FETs. (a) Schematic of top-gated FETs, where 10 nm-thick h-BN nanosheet is capped on top of  $TiS_3$  channel as dielectric. (b) OM image of the device. (c) Current–voltage ( $I_{ds}-V_{ds}$ ) characteristics of device. (d) Transfer ( $I_{ds}-V_{tg}$ ) characteristics for the same device.

510  $mA\ mm^{-1}$ . The two-terminal field-effect mobility can be calculated by the following equation:<sup>24</sup>

$$\mu = \frac{L}{WC_i V_{ds}} \left( \frac{dI_{ds}}{dV_g} \right) \quad (1)$$

where  $L$  and  $W$  are the length and width of the device channel,  $C_i$  is the gate channel capacitance per unit area,  $V_{ds}$  and  $V_g$  are the source–drain and gate voltages. By fitting the linear region of transfer curve, we can estimate that the top-gated  $TiS_3$  FETs have a two-terminal field-effect mobility close to  $100\ cm^2\ V^{-1}\ s^{-1}$  (ESI Fig. S1†). Additionally, the device also exhibits good stability in air condition (ESI Fig. S2†). The excellent electrical performance outstanding in previously reported  $TiS_3$  devices strongly confirms the high crystalline quality of  $TiS_3$  nanosheets, highlighting its potentials for constructing functional electronic devices.<sup>10–12</sup>

We then constructed a planar  $TiS_3-TiO_x-TiS_3$  heterostructure based on the selective oxidation of  $TiS_3$  nanosheet. Selective oxidation of  $TiS_3$  nanosheet was implemented with the assistance of the 532 nm laser equipped on a micro-Raman spectrometer. The laser beam has a spot size of 500 nm, focusing on the surface and scan cross the sample with a grating of 1500 lines per mm. Surface oxidation can be realized under ambient environment due to the local high temperature arised from laser irradiation.<sup>25,26</sup> By setting the scanning rate and size, the surface of  $TiS_3$  nanosheet can be selectively oxidized into  $TiO_x$  to form the in-plane heterostructures (Fig. 3a). Fig. 3b shows the OM image of a  $TiS_3$  nanosheet, in which the surface is selectively oxidated to form a pattern of “HIT”. The pattern can be clearly resolved due to the different light interference from  $TiS_3$  and  $TiO_x$ . From the AFM image shown in Fig. 3c, we can see that laser irradiation causes remarkable change of morphology in  $TiS_3$  nanosheet, and the surface roughness increase significantly from 0.3 to 2.2 nm. It should be noted the pristine  $TiS_3$  without laser irradiation is

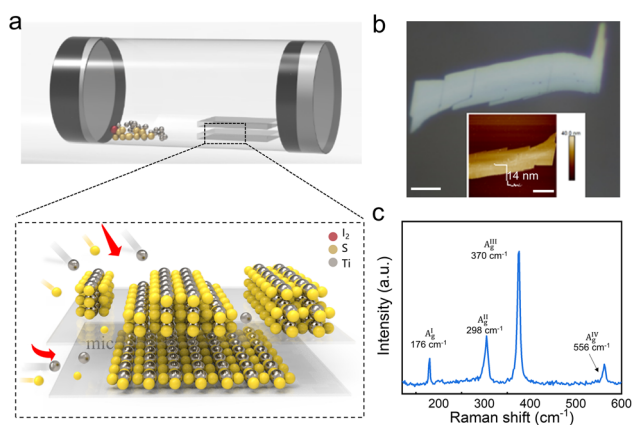
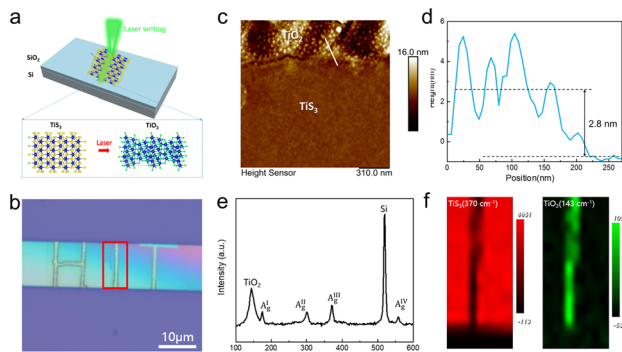


Fig. 1 Synthesis and materials characterization of  $TiS_3$  nanosheets. (a) Schematic of SCCVT to synthesize  $TiS_3$  nanosheets in confined space of mica substates using  $I_2$  as carrier. (b) OM image of  $TiS_3$  nanosheet. The inset image shows the corresponding AFM image. Scale bars: 10  $\mu m$  (c) Raman spectrum collected from  $TiS_3$  nanosheet.





**Fig. 3** Selective oxidation of  $\text{TiS}_3$  nanosheet for constructing in-plane heterojunction. (a) Scheme of laser oxidation from  $\text{TiS}_3$  to  $\text{TiO}_x$ . (b) OM image of a  $\text{TiS}_3$  nanosheet after laser oxidation. (c and d) AFM topography and corresponding height profile of in-plane  $\text{TiS}_3$ - $\text{TiO}_x$  heterojunction. (e) Raman spectrum collected from the oxidized area. (f) The intensity mapping of Raman peaks at  $370$  and  $143\text{ cm}^{-1}$ .

barely affected given the small spot size of laser beam, thus creating a clear border line at the heterojunction area. The Raman spectrum of sample after laser oxidation was collected for comparison<sup>21,27</sup> (Fig. 3d), from which we can clearly resolved an active Raman mode belonging to  $\text{TiO}_2$  at  $143\text{ cm}^{-1}$ . The corresponding intensity mapping images of modes are shown in Fig. 3f. The  $370\text{ cm}^{-1}$  mode of  $\text{TiS}_3$  is barely identified, while the intensity of  $143\text{ cm}^{-1}$  peaks increase significantly. The results strongly confirm the transformation from  $\text{TiS}_3$  to  $\text{TiO}_x$  by laser irradiation and the formation of in-plane  $\text{TiS}_3$ - $\text{TiO}_x$ - $\text{TiS}_3$  heterostructure.

The selective oxidation from  $\text{TiS}_3$  to  $\text{TiO}_x$  can be explained by thermal effect induced by laser irradiation.<sup>26</sup> That is, laser energy absorbed by  $\text{TiS}_3$  would cause the local temperature rise and intense lattice vibration, and  $\text{TiS}_3$  would react with oxygen in ambient environment and be oxidized into  $\text{TiO}_x$ . The local temperature rise is highly related to laser fluence ( $F$ ), and it can be estimated by<sup>28</sup>

$$\Delta T = \frac{S\eta F[1 - \exp(-\alpha d)]}{\rho CV} \quad (2)$$

where  $S$  is the irradiation area,  $\eta$  is the conversion efficiency from light energy to heat,  $V$  is the exposed volume,  $d$ ,  $\rho$  and  $C$  represent the thickness, density, and specific heat of materials, respectively. By combining the material parameters with oxidation condition, we can expect that  $\Delta T$  is estimated in the range from  $300$  to  $500\text{ }^\circ\text{C}$ , which is enough to drive the oxidation reaction in ambient condition.

Two-terminal  $\text{TiS}_3$  device was first fabricated in planar configuration. The channel of device is patterned to  $5\text{ }\mu\text{m}$ , and the center of channel is selectively oxidated by laser irradiation with width of  $1\text{ }\mu\text{m}$ . The resulting  $\text{TiS}_3$ - $\text{TiO}_x$ - $\text{TiS}_3$  heterostructure demonstrates remarkable resistive switching behavior. As shown in Fig. 4a, the channel current continuously increases by six times as applied with 6 consecutives positive voltage sweeps ( $0$ – $3\text{ V}$ ), suggesting the resistance can be effectively modulated through voltage stressing. By applying six consecutive negative voltage sweeps ( $0$  to  $-3\text{ V}$ ), the resistance

would recover back to the initial state (Fig. 4b). The nonlinear modulation of resistance in our memristor is very similar to the transmission characteristics of biological synapses.<sup>29,30</sup> As shown in the inset image of Fig. 4b, the paired electrodes can be treated as the pre- and postsynaptic neurons, and the positive or negative voltage stimulus are used to excite or inhibit the synapses.

Long-term potentiation (LTP) and long-term depression (LTD) characteristic of synapse, which represent the persistent strengthening and weakening of synapses that lead to the long-lasting change of signal transmission between neurons, can also be mimicked by the in-plane memristor. LTP behavior was investigated under 20 identical positive voltage pulse (duration of  $5\text{ ms}$ , amplitude of  $2\text{ V}$ ), and channel current of the device is tracked every  $1\text{ s}$ . For the LTD process, negative voltage pulse (duration of  $1\text{ ms}$ , amplitude of  $-2\text{ V}$ ) was utilized. To exclude the influence of the voltage stressing, we measured the current change with a small reading voltage of  $0.1\text{ V}$ . As shown in Fig. 4c, the conductance and synaptic weight increase gradually under voltage stimulation, with a remarkable change of post-synaptic current (PSC) from  $6$  to  $11\text{ nA}$ . Fig. 4d shows the endurance performance of memristor. We can see that the resistance values for both high resistive state (HRS) and low resistive state (LRS) can be well retained without degradation after  $300\text{ s}$ , indicating good electrical stability of the device. The linear and symmetric conductance update during LTP and LTD are crucial to achieve high learning accuracy for neuromorphic computing.<sup>31,32</sup> The asymmetric ratio ( $A$ ) is defined by the following equation:<sup>33</sup>

$$A = \frac{\max|G_P(n) - G_d(20 - n)|}{G_P(20) - G_d(20)}, (n = 1 - 20) \quad (3)$$

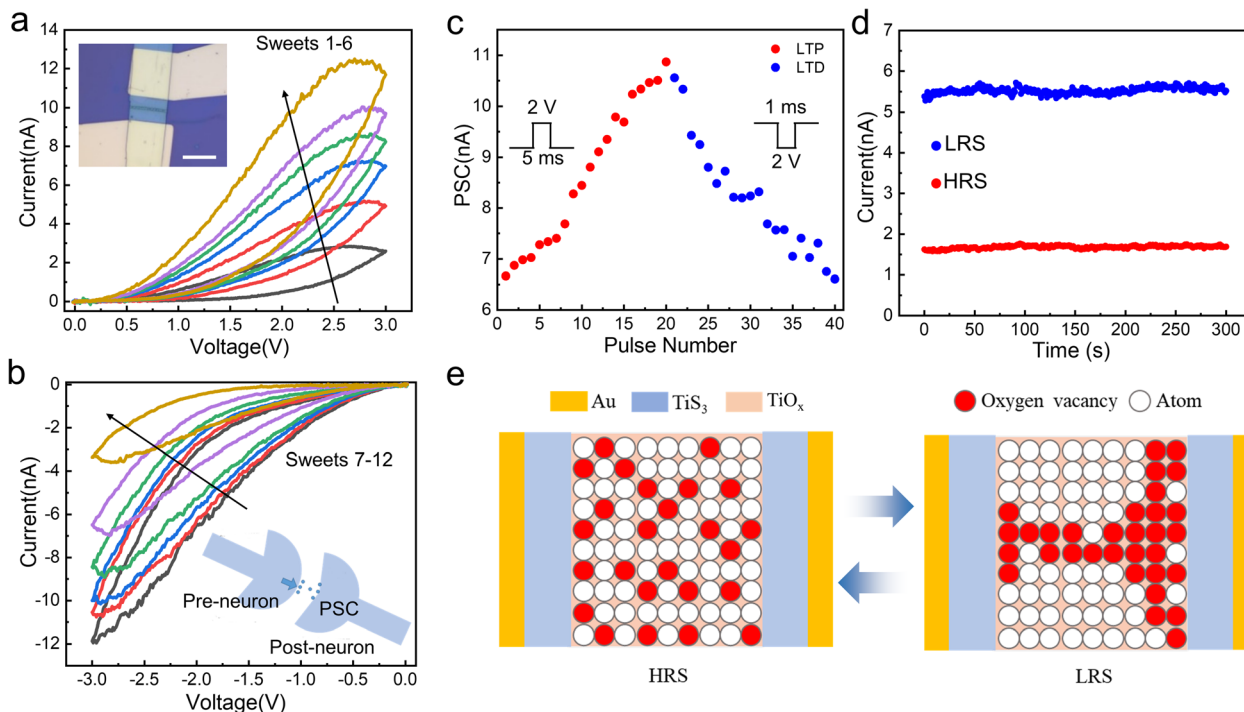
where  $G_P(n)$  and  $G_d(n)$  are the channel conductance values after excitatory or inhibitory pulse, respectively. For our device, a small  $A$  value of  $0.14$  can be obtained, indicating that the device has great potentials for application to achieve high learning accuracy for image recognition.

The modulation mechanism of electrical conductance in  $\text{TiS}_3$ - $\text{TiO}_x$ - $\text{TiS}_3$  planer heterostructure is highly associated with the directional migration and diffusion of oxygen vacancies.<sup>34,35</sup> In the initial HRS, the inherent oxygen vacancies, which introduced during the laser oxidation process, are locally distributed in the  $\text{TiO}_x$  region. These oxygen vacancies can be easily driven under electric field at room temperature, and migrate along channel direction.<sup>17</sup> Meanwhile, the aggregation of oxygen vacancies would contribute to the pathways with high electrical conductivity. The oxygen vacancies acting as n-type dopants would introduce shallow donor states close to the conduction band of  $\text{TiO}_x$ , thus leading to the reduction of barrier height at  $\text{TiO}_x$ - $\text{TiS}_3$  heterojunction and LRS of device<sup>35,36</sup> (ESI Fig. S3†). Therefore, we can expect the effective non-volatile modulation of resistance in our  $\text{TiS}_3$ - $\text{TiO}_x$ - $\text{TiS}_3$  memristor.

The excellent linearity and symmetry in conductance change during long-term potentiation/depression processes enables the device to be integrated into neural network for the high-accuracy pattern recognition. The handwritten letters are resized into  $20 \times 20$  pixels by cropping the edges of the original







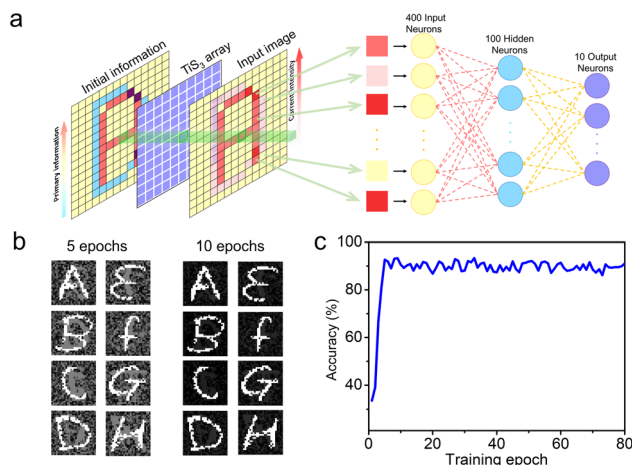
**Fig. 4** The synaptic characteristics of  $\text{TiS}_3\text{-TiO}_x\text{-TiS}_3$  memristor. (a)  $I$ - $V$  characteristics of the memristor at positive bias voltages sweeps. The inset image shows the OM image of a device. (b)  $I$ - $V$  characteristics of the same device at consecutive negative voltages sweeps. Inset image illustrates a biology synapse. (c) Modulation of synaptic weight under positive and negative voltage pulses. (d) Retention performance of the device. The high resistance is identified as the initial state without voltage applying, and low resistance is achieved by consecutively applying 20 positive voltage pulses. (e) Resistance switching mechanism of memristor.

image in Extended Modified National Institute of Standards and Technology (EMNIST) dataset (Fig. 5a). The network consists of 400 input neurons corresponding to  $20 \times 20$  pixels of resized EMNIST image and 10 output neurons with connections through 100 hidden neurons (ESI Fig. S4†). During the simulation, each neuron of input layers represents an

individual device to receive the electrical stimuli corresponding to the grey value of pixel, and transmits the electrical signals to the next layer neurons regarding the conductance status. The updated synaptic weights in network enable output neurons to generate the evolved image. As shown in Fig. 5b, the output digits can be barely distinguishable as trained by 5 epochs. After applied by 10 epochs, synaptic weights were remarkably strengthened, contributing to a much clearer digits with high contrast. The neural network based on our memristor demonstrates a high recognition accuracy of  $\sim 90\%$  with the increasing learning epoch (Fig. 5c). The recognition accuracy is outstanding in previously reported two-terminal resistive switching memoriter and the phase change memory devices.<sup>37–39</sup> The successful emulation of synaptic functions together with high accuracy of image recognition strongly confirm that our  $\text{TiS}_3\text{-TiO}_x\text{-TiS}_3$  in-plane memristor can be utilized for neuromorphic computing applications.

## Conclusions

In summary,  $\text{TiS}_3$  nanosheets with high crystalline quality were synthesized using space-confined vapor transport approach. Based on the samples, we fabricated in-plane  $\text{TiS}_3\text{-TiO}_x\text{-TiS}_3$  heterostructure with the assistance of a laser-assisted manufacture technique. Attributing to directional migration and aggregation of oxygen vacancies, the device demonstrates excellent synaptic characteristics with tunable channel



**Fig. 5** Neuromorphic computing simulation based on the  $\text{TiO}_x\text{-TiS}_3\text{-TiO}_x$  memristor. (a) Schematic diagram of constructed convolutional neural network. (b) Mapping images with different synaptic weight updates as trained for 5 and 10 epochs. (c) The recognition accuracy evolution with training epochs based on our device.



resistance. The excellent multiple resistance levels also allows it to be integrated into neural network for the pattern recognition task, which shows a high recognition accuracy of 90%. Our work provides a simple and effective approach to develop 2D material-based memory and synaptic devices for neuromorphic applications.

## Conflicts of interest

There are no conflicts to declare.

## Acknowledgements

This work was supported by National Natural Science Foundation of China (No. 52102161), Shenzhen Training Programme Foundation for the Innovative Talents (No. RCBS20200714114911270), Natural Science Foundation of Guangdong Province (No. 2021A1515012423), and Stabilization Support Programme of Higher Education Institutes in Shenzhen (No. GXWD20201230155427003-20200805161204001).

## References

- 1 F. Chen, Y. Zhou, Y. Zhu, R. Zhu, P. Guan, J. Fan, L. Zhou, N. Valanoor, F. Von Wegner and E. Saribatur, *J. Mater. Chem. C*, 2021, **9**, 8372–8394.
- 2 Z. Wang, S. Joshi, S. E. Savel'ev, H. Jiang, R. Midya, P. Lin, M. Hu, N. Ge, J. P. Strachan and Z. Li, *Nat. Mater.*, 2017, **16**, 101–108.
- 3 Q. Wan, M. T. Sharbati, J. R. Erickson, Y. Du and F. Xiong, *Adv. Mater. Technol.*, 2019, **4**, 1900037.
- 4 J.-K. Qin, F. Zhou, J. Wang, J. Chen, C. Wang, X. Guo, S. Zhao, Y. Pei, L. Zhen and P. D. Ye, *ACS Nano*, 2020, **14**, 10018–10026.
- 5 M. Si, Y. Luo, W. Chung, H. Bae, D. Zheng, J. Li, J. Qin, G. Qiu, S. Yu and P. Ye, *Presented in part at the 2019 IEEE International Electron Devices Meeting, IEDM*, 2019.
- 6 P. Yao, H. Wu, B. Gao, J. Tang, Q. Zhang, W. Zhang, J. J. Yang and H. Qian, *Nature*, 2020, **577**, 641–646.
- 7 W. Huh, D. Lee and C. H. Lee, *Adv. Mater.*, 2020, **32**, 2002092.
- 8 J. K. Qin, B. X. Zhu, C. Wang, C. Y. Zhu, R. Y. Sun, L. Zhen, Y. Chai and C. Y. Xu, *Adv. Electron. Mater.*, 2022, **8**, 2200721.
- 9 J. Lao, W. Xu, C. Jiang, N. Zhong, B. Tian, H. Lin, C. Luo, J. Travas-sejdic, H. Peng and C.-G. Duan, *J. Mater. Chem. C*, 2021, **9**, 5706–5712.
- 10 J. O. Island, M. Barawi, R. Biele, A. Almazán, J. M. Clamagirand, J. R. Ares, C. Sánchez, H. S. Van Der Zant, J. V. Álvarez and R. D'Agosta, *Adv. Mater.*, 2015, **27**, 2595–2601.
- 11 J. O. Island, R. Biele, M. Barawi, J. M. Clamagirand, J. R. Ares, C. Sánchez, H. S. van der Zant, I. J. Ferrer, R. D'Agosta and A. Castellanos-Gomez, *Sci. Rep.*, 2016, **6**, 22214.
- 12 N. Tripathi, V. Pavelyev, P. Sharma, S. Kumar, A. Rymzhina and P. Mishra, *Mater. Sci. Semicond. Process.*, 2021, **127**, 105699.
- 13 J.-K. Qin, H.-L. Sun, T. Su, W. Zhao, L. Zhen, Y. Chai and C.-Y. Xu, *Appl. Phys. Lett.*, 2021, **119**, 201903.
- 14 G. Zhou, B. Sun, X. Hu, L. Sun, Z. Zou, B. Xiao, W. Qiu, B. Wu, J. Li and J. Han, *Adv. Sci.*, 2021, **8**, 2003765.
- 15 T. Dongale, N. Desai, K. Khot, C. Volos, P. Bhosale and R. Kamat, *J. Nanoelectron. Optoelectron.*, 2018, **13**, 68–75.
- 16 M. K. Akbari, R. K. Ramachandran, C. Detavernier, J. Hu, J. Kim, F. Verpoort and S. Zhuiykov, *J. Mater. Chem. C*, 2021, **9**, 2539–2549.
- 17 B. Zhao, M. Xiao and Y. N. Zhou, *Nanotechnology*, 2019, **30**, 425202.
- 18 L. Liu, Z. Cheng, B. Jiang, Y. Liu, Y. Zhang, F. Yang, J. Wang, X.-F. Yu, P. K. Chu and C. Ye, *ACS Appl. Mater. Interfaces*, 2021, **13**, 30797–30805.
- 19 Y. Li, J. Yang, Z. Zhan, J. Wu, H. Li, L. Zhen, Q. He and C. Xu, *Sci. China: Technol. Sci.*, 2020, **63**, 1531–1537.
- 20 B. Wang, H. Luo, X. Wang, E. Wang, Y. Sun, Y.-C. Tsai, J. Dong, P. Liu, H. Li and Y. Xu, *Nano Res.*, 2020, **13**, 2035–2043.
- 21 A. Lipatov, M. J. Loes, H. Lu, J. Dai, P. Patoka, N. S. Vorobeva, D. S. Muratov, G. Ulrich, B. Kästner and A. Hoehl, *ACS Nano*, 2018, **12**, 12713–12720.
- 22 A. S. Pawbake, J. O. Island, E. Flores, J. R. Ares, C. Sanchez, I. J. Ferrer, S. R. Jadhkar, H. S. Van Der Zant, A. Castellanos-Gomez and D. J. Late, *ACS Appl. Mater. Interfaces*, 2015, **7**, 24185–24190.
- 23 A. Khatibi, R. H. Godiksen, S. B. Basuvalingam, D. Pellegrino, A. A. Bol, B. Shokri and A. G. Curto, *2D Mater.*, 2019, **7**, 015022.
- 24 H. H. Choi, K. Cho, C. D. Frisbie, H. Sirringhaus and V. Podzorov, *Nat. Mater.*, 2017, **17**, 2–7.
- 25 C. Tan, Y. Liu, H. Chou, J.-S. Kim, D. Wu, D. Akinwande and K. Lai, *Appl. Phys. Lett.*, 2016, **108**, 083112.
- 26 Z.-Q. Xu, Y. Zhang, Z. Wang, Y. Shen, W. Huang, X. Xia, W. Yu, Y. Xue, L. Sun and C. Zheng, *2D Mater.*, 2016, **3**, 041001.
- 27 H. C. Choi, Y. M. Jung and S. B. Kim, *Vib. Spectrosc.*, 2005, **37**, 33–38.
- 28 R. S. Singh, V. Nalla, W. Chen, A. T. S. Wee and W. Ji, *ACS Nano*, 2011, **5**, 5969–5975.
- 29 Z. Q. Wang, H. Y. Xu, X. H. Li, H. Yu, Y. C. Liu and X. J. Zhu, *Adv. Funct. Mater.*, 2012, **22**, 2759–2765.
- 30 Z. I. Mannan, S. P. Adhikari, C. Yang, R. K. Budhathoki, H. Kim and L. Chua, *IEEE Trans. Neural Netw. Learn. Syst.*, 2019, **30**, 3458–3470.
- 31 S. Ambrogio, P. Narayanan, H. Tsai, R. M. Shelby, I. Boybat, C. Di Nolfo, S. Sidler, M. Giordano, M. Bodini and N. C. Farinha, *Nature*, 2018, **558**, 60–67.
- 32 S. Seo, B.-S. Kang, J.-J. Lee, H.-J. Ryu, S. Kim, H. Kim, S. Oh, J. Shim, K. Heo and S. Oh, *Nat. Commun.*, 2020, **11**, 3936.
- 33 C. S. Yang, D. S. Shang, N. Liu, E. J. Fuller, S. Agrawal, A. A. Talin, Y. Q. Li, B. G. Shen and Y. Sun, *Adv. Funct. Mater.*, 2018, **28**, 1804170.
- 34 J. Kwon, A. A. Sharma, J. A. Bain, Y. N. Picard and M. Skowronski, *Adv. Funct. Mater.*, 2015, **25**, 2876–2883.
- 35 J. J. Yang, M. D. Pickett, X. Li, D. A. Ohlberg, D. R. Stewart and R. S. Williams, *Nat. Nanotechnol.*, 2008, **3**, 429–433.
- 36 D. S. Hong, Y. S. Chen, J. R. Sun and B. G. Shen, *Adv. Electron. Mater.*, 2016, **2**, 1500359.



- 37 G. W. Burr, R. M. Shelby, S. Sidler, C. Di Nolfo, J. Jang, I. Boybat, R. S. Shenoy, P. Narayanan, K. Virwani and E. U. Giacometti, *IEEE Trans. Electron Devices*, 2015, **62**, 3498–3507.
- 38 Y. Zhang, Y. Li, X. Wang and E. G. Friedman, *IEEE Trans. Electron Devices*, 2017, **64**, 1806–1811.
- 39 M. Khalid, *IEEE Trans. Electr. Electron. Mater.*, 2019, **20**, 289–298.

